UNIVERSITY OF CALIFORNIA, IRVINE

Fluorescence Lifetime Imaging Microscopy and LAURDAN Spectral Imaging for Dynamically Investigating Osteoclast Differentiation

THESIS

Submitted in partial satisfaction of the requirement for the degree of

MASTER OF SCIENCE

In Biomedical Engineering

by

Dean G. Nguyen

Thesis committee:
Associate Professor Michelle A. Digman, chair
Professor Enrico Gratton
Associate professor Wendy Liu

2020

DEDICATIONS

To my friends and family, especially to my parents who, in their 60s, decided to leave their lives in Vietnam behind and came to America, so I have a chance to be someone.

TABLE OF CONTENTS

LIST OF FIGURES

ACKNOWLEDGEMENT

I would love to express my sincere gratitude towards my advisor, Dr Michelle A. Digman, and my committee members Dr. Enrico Gratton, and Dr. Wendy Liu. Dr. Digman has been guiding me through graduate school with so much patience and understanding, and Dr. Enrico Gratton has been providing me with so many valuable advices. It was a great honor to be a part of the Digman lab as well as the Laboratory for Fluorescence Dynamics. I also want to thank Dr. Wendy Liu for graciously agreeing to be part of my thesis committee.

I want to acknowledge my collaborator Dr. Haibo Zhao for training on osteoclasts culture and providing many needed materials. I also want to thank Dr. Ning Ma and the rest of the Digman lab / LFD for providing training and advices on imaging techniques and analysis.

ABSTRACT OF THE THESIS

Fluorescence Lifetime Imaging Microscopy and LAURDAN Spectral Imaging

for Dynamically Investigating Osteoclast Differentiation

by Dean G. Nguyen

Master of Sciences in Biomedical Engineering

University of California, Irvine, 2020

Associate Professor Michelle Digman, Chair

Osteoclasts, the multinucleated bone-resorbing cells, are involved in the destructive breakdown of bones in many diseases such as osteoporosis and rheumatoid arthritis. Designing an efficient and specific therapeutic strategy to these diseases would depend on understanding osteoclasts differentiation. Although gene expression quantification and biochemical techniques have been used extensively to study osteoclast differentiation, they lack the capability to dynamically examine live osteoclasts at the single-cell level. In this thesis, we explored the practicality of the two minimally invasive microscopy techniques, NAD(P)H Fluorescence Lifetime Imaging and LAURDAN spectral imaging, in observing cellular metabolic profiles and membrane dynamics respectively during osteoclast differentiation. In addition to establishing the practicality of these two imaging platforms, our report offered a deeper understanding regarding the roles of metabolism and membrane dynamics in osteoclasts differentiation and pathogenesis of osteoclasts-associated diseases.

Chapter 1: Backgrounds on osteoclasts

The skeletal system gives the human body mechanical support, storage of calcium and phosphate. Though out the lifetime of a human, bones are constantly remodeled to allow growth and maintain homeostasis. The remodeling process of bones are carried out by two cell types: osteoblasts and osteoclasts, which form and breakdown the bone matrix respectively. Any imbalance between bone formation and resorption would lead to abnormally soft or brittle bones. Although bone remodeling depends on both osteoblast and osteoclast, most of the known bone diseases are caused by excess or insufficient activity of osteoclasts. Those diseases range from the systemic osteoporosis and osteopetrosis, to the localized bone destruction in rheumatoid arthritis [1]. Osteoclasts are large multinucleated cells that belong the myeloid lineage of leukocytes. The differentiation of osteoclast involves many steps which begin with formation of common myeloid progenitor cells from hemopoietic stem cells under the influence of many factors such as IL-3 and IL-6 [2]. If stimulated by macrophage colony stimulating factor (M-CSF), these cells will further differentiate into monocyte/macrophage lineage cells. Monocytes can either cross the bone lining monolayer from the bone marrow or from blood into the bone remodeling compartment (BRC) where they are exposed to RANKL (Receptor Activator of NfKB ligand) and begins differentiating toward mature osteoclasts. The RANKL-stimulated cells then spend some time in a transient state called pre-osteoclasts before fusing with one another to form mature multinucleated osteoclasts [3] (Figure 1A) . Although M-CSF and RANKL are the two key factors for osteoclast differentiation, survival, function, other factors such as proinflammatory TNFα and Il-1β were reported to possibly accelerate differentiation and bone resorption activity [4,5]. Bone resorption starts with mature osteoclasts

forming a strong attachment with the bone surface in the BRC via integrin-osteopontin interaction. The cells then seal off the microenvironment between its apical side and the bone surface by forming more attachments. Afterward, proton and digestive enzymes like cathepsin K are secreted to dissolve the bone mineral and the collagen matrix respectively. The resorption products (calcium and phosphate ion, protein fragments) are then transported to the basolateral side via transcytosis to prevent toxic buildup (Figure 1B) [6].

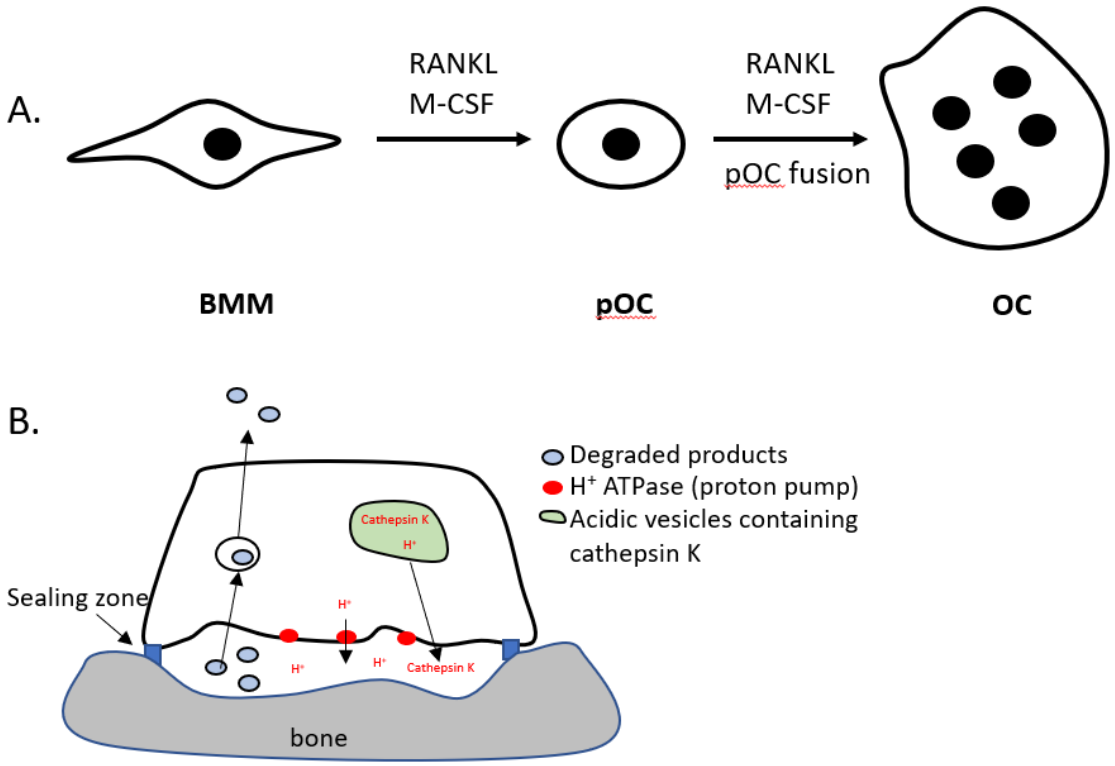

Figure 1: Osteoclast differentiation and bone resorption. A. Osteoclast differentiation depends on both M-CSF and RANKL. BMM, bone marrow monocyte. pOC, pre-osteoclast. OC, mature osteoclasts. B. A simplified model of bone resorption activity.

Chapter 2: Investigating the metabolic profile of osteoclasts and its precursors using NAD(P)H FLIM

2.1 Introduction

Osteoclast differentiation and metabolism

ATP, the energy currency of cells, is synthesized through two distinct processes: glycolysis and mitochondrial oxidative phosphorylation. In hypoxic environment, there would be inadequate oxygen to act as the final electron acceptor for mitochondrial oxphos; thus, most cells would shift toward a more glycolytic metabolism. However, some cells can also undergo a process known as aerobic glycolysis, also known as the Warburg effect, in which they prefer glycolysis even in normoxic condition[7]. Studies on metabolism-related genes demonstrated that both glycolysis and oxidative phosphorylation are of critical importance to osteoclast differentiation and function [8–12]. Both osteoclastogenic differentiation and bone resorption are energy-expensive processes. In order to adapt to increased demand of ATP, differentiating cells might have to alter their cellular metabolic profile. However, we still know very little about the how the metabolic profile of cells at different stage of osteoclastogenesis differ from each other's. Thus, we aimed at examining the change of cellular metabolic state throughout osteoclastogenesis using the NAD(P)H Fluorescence lifetime imaging microscopy (FLIM) technique coupled with phasor analysis in this study. NAD(P)H FLIM is a powerful single cell analysis technique that allows dynamic observation of live cells. In contrast, conventional methods to study the cellular metabolic states such as assessing gene expression, measuring metabolite in spent media, or quantifying oxygen consumption through SEAHORSE assay are

bulk analysis methods that completely overlook the heterogeneity within a culture, while also lacking the capability to assess the dynamics of subcellular distribution [13,14]. Our data demonstrated the practicality of the NAD(P)H FLIM in studying cellular metabolism while giving us better understanding about the alteration of metabolic profile during osteoclast differentiation, allowing potential design of therapeutic strategy in the future.

2.2 Osteoclasts-associated disease models: iron transport perturbation and TNFα exposure

Furthermore, we also wanted to use NAD(P)H FLIM to examine possible alteration of cellular metabolic profile of osteoclast disease models: iron transport perturbation and exposure to the inflammatory cytokine TNFα. Despite its indispensable role in cellular metabolism, excess amount of intracellular iron might alter the metabolic program, stimulate generation of reactive oxygen species, and disrupt signaling pathways [15,16]. In fact, perturbation of iron uptakes is known to cause a variety osteoclast-mediated bone diseases [17,18]. In this report, we used *Ferroportin* knockout (*fpn* KO) and *Transferrin Receptor 1* knockout (*tfr1* KO) cells as out iron transport perturbation models. Outward transport through FPN, along with other processes, ensure that the level of iron inside cells would not build up to an abnormal level; thus, loss of *fpn* would result in a rise of intracellular iron (Figure 2). In contrast, the loss of *tfr*1 would cause a decrease in intracellular iron (Figure 2). A prior study and unpublished data from our collaborator demonstrated that conditional deletion of *fpn* and *tfr1* in mice caused osteoporosis and osteopetrosis respectively [19]. Next, we examined the metabolic alteration of mature osteoclast exposed to TNFα because this proinflammatory cytokine is involved in rheumatoid arthritis and periodontal disease [20,21]. TNFα is also known to accelerate both osteoclast differentiation and bone resorption activity [4,5]. Our report would supplement

understandings of the pathogenesis of various bone diseases, while demonstrating the potential of NAD(P)H FLIM as a diagnostic platform.

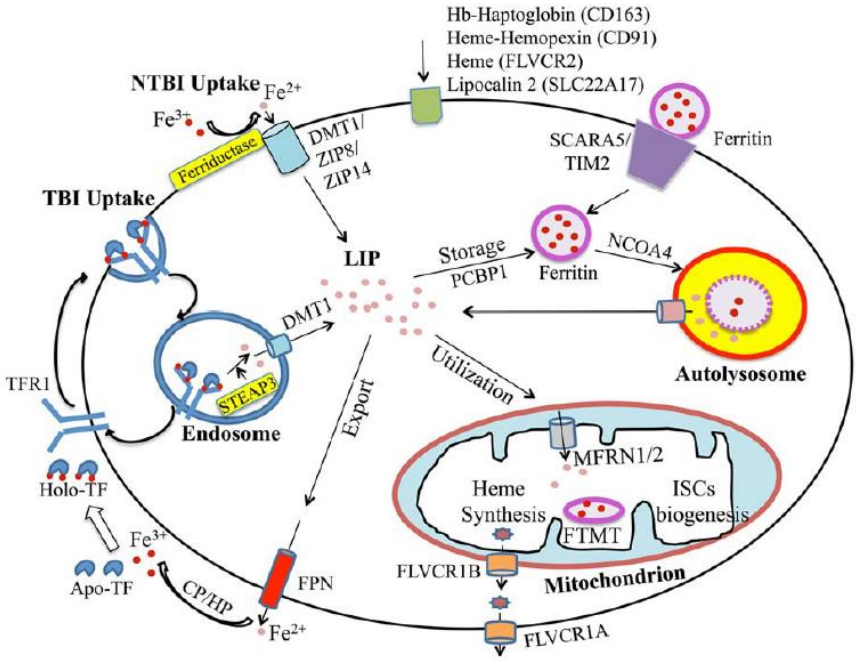

Figure 2: Overview of cellular iron uptakes and utilization. Iron is imported, exported, sequestered, and sequestered through many different pathways. Drawing was adapted from Dev *et al* [22].

2.3 Fluorescence lifetime imaging microscopy

Fluorescence lifetime imaging microscopy is a very versatile tool that has been widely used to study many cellular processes including metabolism [23–25]. The fluorescence lifetime of a population of fluorophore is the time it takes for the number of the excited molecules, which is proportional to the intensity, to decrease to 36.8% (or 1/e) of its original value. The lifetime does not depend on the concentration of said fluorophore but is characteristic of its conformation and environment.

$$I(t) = \alpha e^{-t/\tau} \quad (1)$$

Equation (1) represents a decay with a single exponential term. If the decay involves multiple exponential terms, it can be represented by the following equation:

$$I(t) = \Sigma_i \alpha_i e^{-t/\tau_i} \quad (2)$$

Conventionally, FLIM data has been collected using the time correlated single photon counting (TCSPC) technique and analyzed by fitting the decay at each pixel into one or two exponents. However, the low photon counts at each pixel would make it difficult to perform accurate fitting. Besides, fitting the decay of every single pixel of an image having up to 10^5 pixels might require an immense amount of computational power. In this study, we instead utilized the phasor transformation which can substantially simplify the analysis. By transforming the data into the phasor space, a global view of the fluorescence decay at each pixel of the image can be provided without any complicated fitting procedure [25]. If the data is collected through the TCSPC technique, the histogram of photon arrival time at each pixel can be transformed as follow:

$$g(\omega) = \frac{\int_0^\infty I(t)\cos(\omega t)dt}{\int_0^\infty I(t)dt} \quad (3)$$

$$s\ (\omega) = \frac{\int_0^\infty I(t)\cos(\omega t)dt}{\int_0^\infty I(t)dt} \quad (4)$$

Where ω = 2πf, and f = 1/T or the laser repetition rate. If the data is collected in the frequency domain, the following transformation can be used instead:

$$g(\omega) = Mcos(\phi)$$

$$s(\omega) = Msin(\phi)$$

In which M and ϕ are modulation and phase shift respectively. Combining equation (1) with equation (3) and (4), and then solving the integration, we can express the equation of g and s in terms of lifetime if the decay only has one exponential term:

$$g(\omega) = \frac{1}{1+(\omega t)^2}$$

$$s(\omega) = \frac{\omega t}{1+(\omega t)^2}$$

The last 2 equation can be derived into the following equation:

$$s^2 + (g - 0.5)^2 = 0.25$$

Which means all the monoexponential decays would fall on top of a universal circle which centers at (0.5, 0) and has a radius of 0.5. A short lifetime would lie closer to the (1,0) point which is equivalent to τ = 0, while a longer lifetime would lie near the (0,0) point which corresponds to τ = ∞. Another important characteristic of the phasor technique is the rule of linear addition. A phasor plot of any mixtures of two exponential species will fall on the straight line connecting the two positions of each of the pure single exponential, which are on the universal semicircle [26] (figure 3C). The exact position of the mixture on this line is determined by the fractional contributions, as represented by the following equation:

$$G(w) = \Sigma\, f_n g_n(w)$$

$$S(w) = \Sigma\, f_n s_n(w)$$

In which f is the fractional contribution. In a two-components system, the g coordinate of the mixture equals to the sum of the products between the g coordinate of component 1 and 2 and its respective fractional contributions.

2.4 NAD(P)H fluorescence lifetime

NADH is a key compound in cellular respiration because it acts as the major electron carrier. When cells favor glycolysis, the amount of NADH produced by glycolysis and TCA cycle would exceed the amount of NADH oxidized into NAD^+ in the mitochondria, resulting in increased NADH/ NAD^+ ratio. Many conventional assays that can directly measure the NADH/ NAD^+ ratio has been used widely to study cellular metabolism. However, they usually involve lysing or fixing the tissue culture, making them incompatible to observing the dynamics of living cells [27–29]. Instead of relying on these invasive assays to study cellular metabolic profiles, many studies used the fluorescence lifetime imaging microscopy technique to quantitatively assessing the ratio of free to protein-bound NADH instead [23,24]. Both free and bound NADH are autofluorescent, with absorption peaks at 350 nm, and emission peaks at 450 nm [30]. Free NADH has a closed conformation causing it to quench its own fluorescence, resulting in a short lifetime at 0.4 ns. However, the bound form of NADH has a longer lifetime at around 3.4 ns because of its open conformation (figure 3A, B). Although NADH absorption peaks in the UV range, which is highly damaging to cells and tissue, this problem is overcome by using two-photon excitation instead. Two-photons excitation also comes with the added benefit of having lower scattering, and better sectioning capability in comparison to one photon excitation[31].

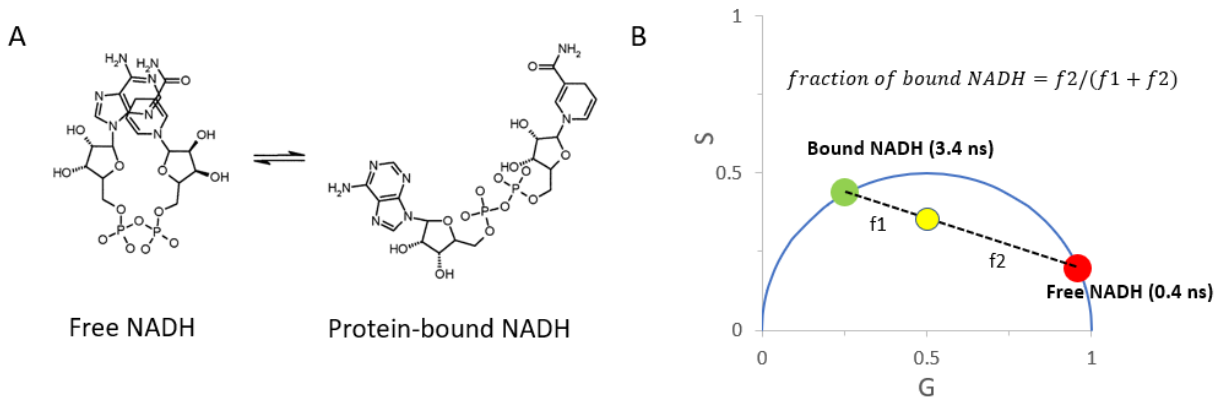

Figure 3: NAD(P)H Fluorescence Lifetime. A. Close conformation of free NADH and open conformation of bound NADH, drawing adapted from Hull *et al* [32]. B. Phasor positions of free and bound NADH (if laser repetition rate = 80 MHz) and the equation to calculate the fraction of bound NADH. Yellow dot represents a hypothetical position of a mixture of free and bound NADH.

2.5 Materials and methods

Animals

All experiments on mice were approved by Long Beach Veteran Affairs Hospital.

Bone marrow macrophage collection

Whole bone marrow was extracted from 8-10 weeks old WT, *fpn* conditional knockout (FPN-flox LysM-Cre), and *tfr1* conditional knockout mice (TFR1-flox LysM-Cre). After removal of tissue debris by cell strainers, red blood cells were lysed using the following buffer for 5 minutes at room temperature: 150 nM NH_4Cl, 10 mM $KNCO_3$, 0.1 mM EDTA, pH 7.4. Bone marrow cells were plated onto a 100 mm petri-dish and cultured in α-10 medium (α-MEM medium, 10% endotoxin-free heat-inactivated fetal bovine serum, 1 x Penicillin-Streptomycin-L-Glutamine solution) containing 1/10th volume of CMG 14-12 (conditioned medium supernatant containing recombinant M-CSF at 1 ug/mL) for 4 to 5 days. During this period, the cell culture media was changed with fresh α-10 medium and CMG 14-12 every other day. Finally, the

resulting bone marrow monocytes (BMM) were collected and frozen in FBS, 10% sterile DMSO for later uses.

Osteoclast culture and differentiation

WT, *fpn* KO, and *tfr1* KO cells were thawed and let recover in α-10 media with $1/10^{th}$ CMG for four days. Fresh media and CMG were changed every other day in this step as well. Then, cells were trypsinized, collected, and plated onto 35 mm imaging dishes (Ibidi, volume = 2 mL, coverslip thickness = 0.17 mm) at the density of $13*10^4$ cells / dish in α-10 media. To initiate osteoclast differentiation, α-10 media was also supplemented with both $1/100^{th}$ CMG 14-12 and 100 ng/mL RANKL. A few imaging dishes were supplemented with only $1/100^{th}$ CMG 14-12 but not RANKL, so that those cells would maintain the monocytic fate while stopping cell division. Both bone marrow monocytes (BMM) and pre-osteoclasts (pOC) were imaged two days after plating, while mature osteoclast (OC) would only appear in sufficient number for imaging four days after start of RANKL treatment.

FLIM data acquisition

Fluorescence lifetime images of this study were acquired on a laser scanning microscope Olympus Fluoview FV1000 system coupled with a Titanium: sapphire laser (Spectra-Physics Mai Tai, Mountain View, CA, USA) that has an 80 MHz repetition rate. The fluorescence from the samples were detected by external photomultiplier tubes (H7422p-40, Hamamatsu, Japan), which transferred data to a phasor plot via an a320 FastFLIM FLIMbox (ISS, Champaign, IL, USA). The cells were excited at 740 nm; an average power of 3 mW laser power was used to ensure low phototoxicity [33]. The objective used for all data acquisition was an Olympus UPlanSAPO 60x/1.2 NA water objective. The following settings were used for FLIM data collection: image

size 256 x 256 pixels, laser dwell time = 20 us/pixel, 50 frames per image. A 690 nm dichroic filter was used to separate the emitted fluorescence from the excitation laser. Additionally, the emitted fluorescence was split into two with a 496 nm LP filter; one path went through a 460/80 bandpass filter while the other through a 540/50 filter before hitting their photomultiplier tubes. However, only the blue channel (460/80) was used for data analysis. Calibration was performed by acquiring FLIM data on coumarin6 (dissolved in pure ethanol), a fluorophore that has a known lifetime of τ = 2.5 ns [25]. Throughout the entire imaging sessions, the cells were kept in standard culture condition using the incubation system of FV1000: 37^{o}C, 5% CO_2, 20% O_2, with enough humidity. FLIM data was acquired and processed using the program SimFCS developed at the laboratory for fluorescence dynamics.

Phasor analysis of FLIM data

FLIM data was transformed into the phasor space using SimFCS which performed the transformation equation mentioned earlier. Individual cells are selected, and nuclei regions were excluded using the masking function of SimFCS prior to calculating NAD(P)H fraction bound in the cytoplasm. However, nuclei were left on the images when preparing the representative images (FLIM map) for aesthetic reason. Fraction of bound NADH was calculated by projecting the phasor distribution onto the free-bound line, and then calculated the center of mass of the resulting histogram.

2.5 Results

1. WT, *fpn* KO, *tfr1* KO cells NADH FLIM during differentiation

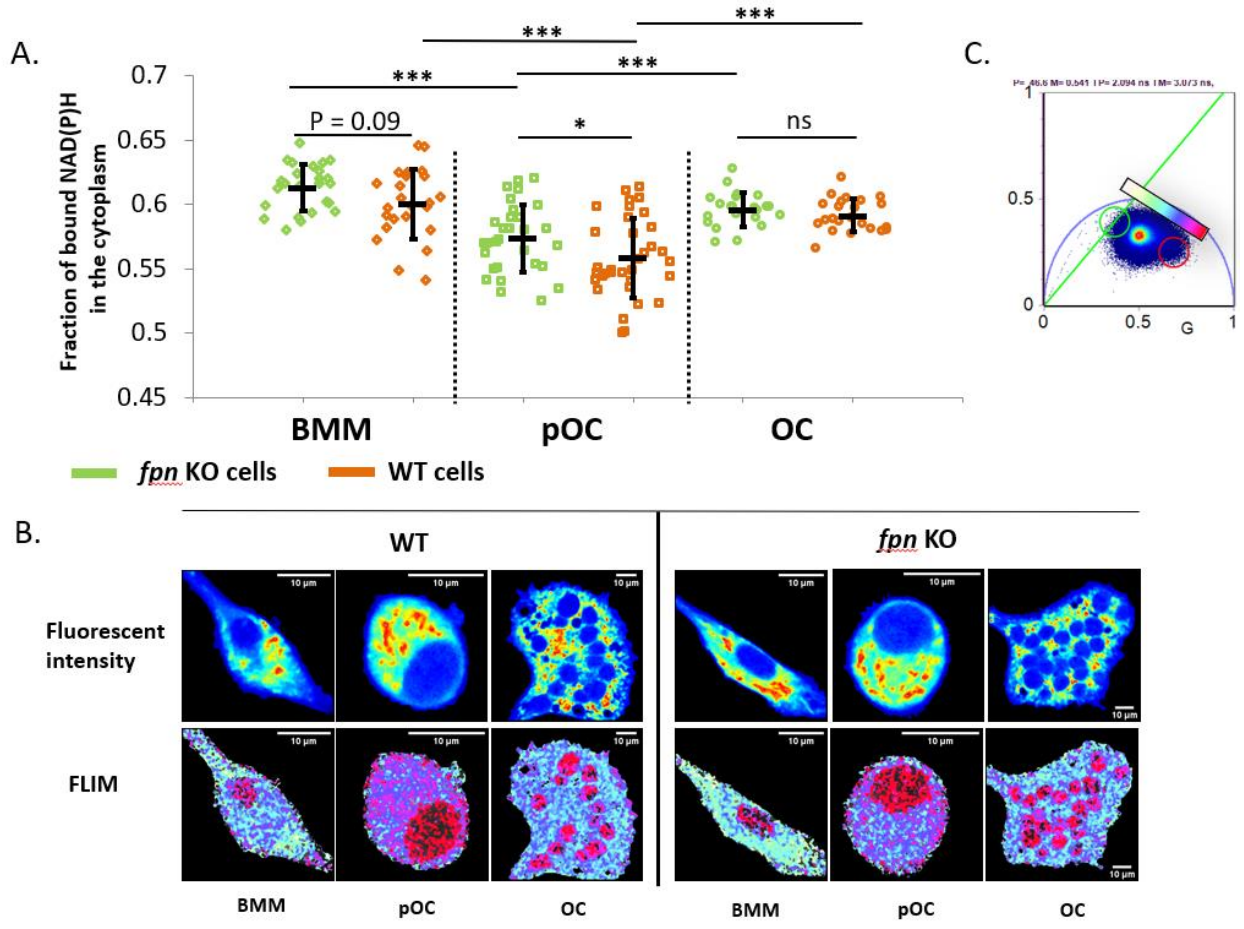

Figure 4: NAD(P)H FLIM data of *fpn* KO and WT cells during osteoclast differentiation. A. Fraction of bound NAD(P)H in the cytoplasm, each data points represent the average fraction of bound NAD(P)H in the cytoplasm of one cell. B. Fluorescent intensity and FLIM images. C. Phasor plot and the color scale for constructing FLIM images. Error bars: Standard deviation. Mann-Whitney U test. *, $p < 0.05$; **, $p < 0.01$; ***, $p < 0.001$; ns, $p > 0.5$. n= 25-30 cells / group. 2 independent experiments.

WT, *fpn* KO (*ferroportin* knockout), and *tfr1* KO (transferrin1 knockout) bone marrow monocytes (BMM) cells were stimulated with RANKL and CMG (recombinant M-CSF) to initiate osteoclast differentiation. The cells undergoing differentiation (pre-Osteoclast or pOC) were imaged 2 days after the start of RANKL stimulation. BMM, which were not exposed to RANKL

but only CMG to maintain the monocytic fate, were also imaged in the same day as pOC. At this point, there was no multinucleated cells yet. pOCs had the rounded morphology consistent with other studies [3]. After 4 days of RANKL exposure, large multinucleated OCs were available for imaging. Figure 4C and 5C shows the phasor plot of cells in their respective experiments with each dot represents the fluorescent decay at one pixel. To construct the FLIM images, a color scale was placed on top of the line connecting free to bound NAD(P)H lifetime on the phasor. If the phasor position of a pixel lied on a certain color patch, this pixel would take on said color in the FLIM image. On this color scale, the pink color was closer to the free NAD(P)H position of the universal circle (0.4 ns) Thus, pink and deep blue color corresponded to higher contribution of free NAD(P)H, while white and cyan corresponded to higher contribution of bound NAD(P)H due to being near the pure bound NAD(P)H position (figure 4C, 5C). Consistent with prior studies, the FLIM images showed that nuclei contained mainly free NAD(P)H (figure 4B, 5B, 6B) [34]. Because major cellular bioenergetic pathways take place in the cytoplasm, the nuclei area in the images were excluded before calculating the average fraction of bound NAD(P)H. In all three genotypes, the cytoplasm of pOCs was predominantly pink and deep blue while the cytoplasm of BMMs was predominantly cyan and white (figure 4B, 5B). Likewise, the fraction of bound NAD(P)H of pOC were lower in comparison to BMMs regardless of genotypes (figure 4A, 5A), suggesting that there could be a shift toward glycolysis when cells underwent differentiation. The fraction of bound NAD(P)H in the cytoplasm of OCs were higher than pOC, and the cytoplasmic area of FLIM images of OCs were mainly cyan and white. Therefore, it is probable that cells shifted to a more glycolytic state during osteoclast differentiation and shifted back toward a more oxphos dominant program upon reaching the mature osteoclast

stage.

2. Comparing WT cells NAD(P)H FLIM to *fpn* KO cells and *tfr1* KO cells

To further elucidate the role of iron on osteoclasts' metabolism, we used two gene knockout models in this study: *fpn* and *tfr1* KO. FPN transports excess iron out of the cell though it is not the only mechanisms that reduces surplus iron (figure 2). Loss of *fpn* is supposed to cause a slight increase of intracellular iron [19]. However, there was no difference in fraction of bound NAD(P)H between WT and *fpn* KO cells in the BMM and OC stages. Only at the pOC stage, the cytoplasm of *fpn* KO cells had a roughly 2% higher fraction of bound NAD(P)H relative to WT on average (figure 4A), but this difference did not look obvious in the FLIM images (figure 4B).

TFR1 imports iron into cells though endocytosis of transferrin-Fe complex. Although *tfr1* deletion might cause a decrease in intracellular iron, *tfr1* KO cells would not be completely iron-starved due to presence of other iron import mechanisms (figure 2). Like the comparison between *fpn* KO and WT cells, there were no difference between the cytoplasmic fraction of bound NAD(P)H of *tfr1* KO cells and WT cells. Only during the pOC stage, fraction of bound NAD(P)H in the *tfr1* KO cells was lower than WT by roughly 2% (figure 5 A, B).

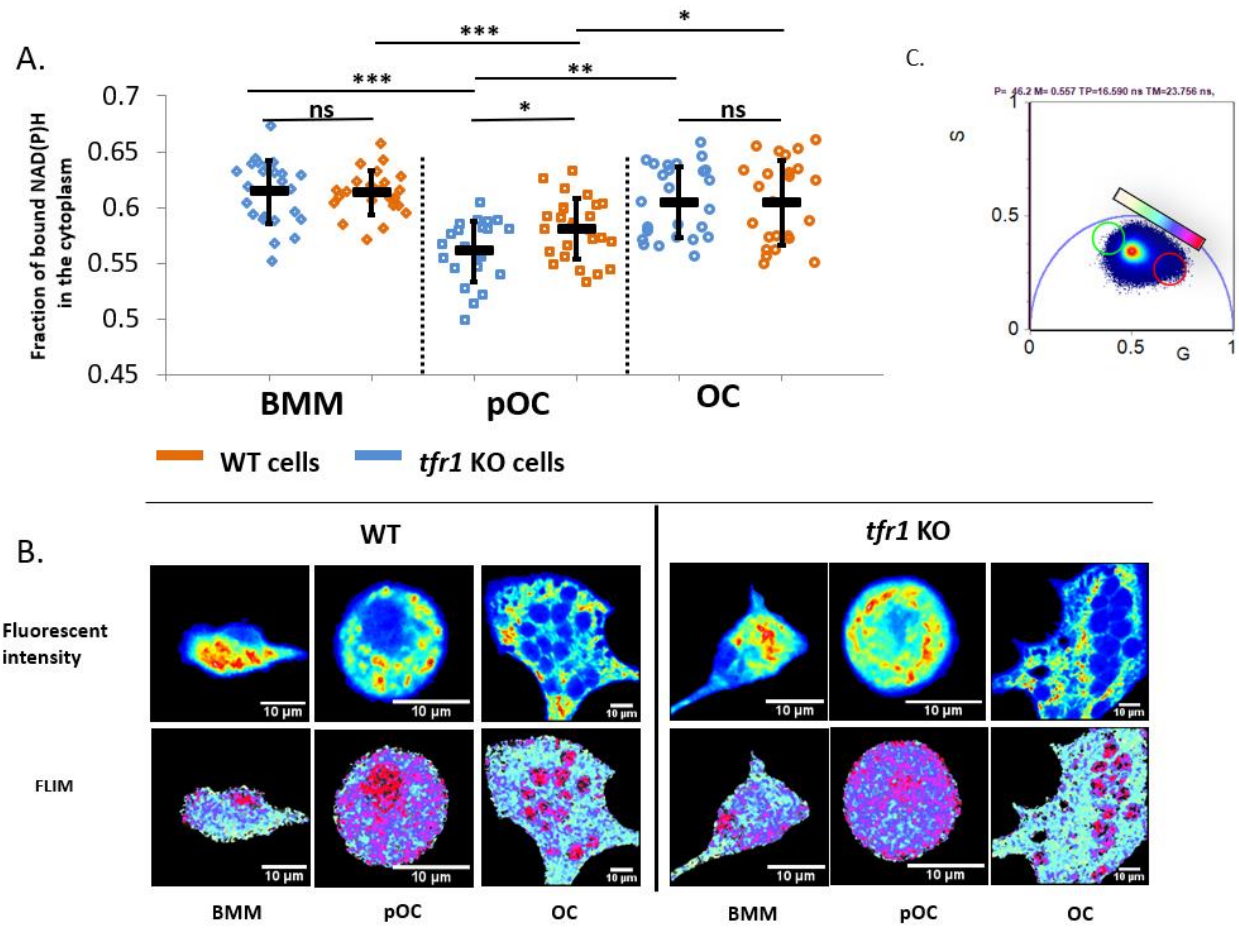

Figure 5: NAD(P)H FLIM data of WT and *tfr1* KO cells during osteoclast differentiation. A. Fraction of bound NAD(P)H in the cytoplasm of WT and *tfr1* KO cells at different stages of differentiation. Each data point represents the cytoplasm of one cell. B. Fluorescent intensity and FLIM images of some representative cells. C. Phasor plot and the color scale for constructing the FLIM images. Mann-Whitney U test. *, $p < 0.05$; **, $p < 0.01$; ***, $p < 0.001$; ns, $p > 0.5$. n= 20-30 cells / group. 2 independent experiments.

3. Effects of the proinflammatory cytokine TNFα on the NADH FLIM signal of mature WT osteoclasts

Many inflammatory diseases such as periodontal infection or rheumatoid arthritis can lead to severe osteoclasts-mediated bone destruction [35]. The inflammatory cytokine tumor necrosis factor alpha (TNFα) has been documented to accelerate osteoclastogenesis through both RANK dependent and independent pathway [36,37]. However, its direct action on mature

multinucleated osteoclasts is much less clear. One neat thing about FLIM is its potential to identify cellular subtypes based on their phasor position without use of dyes or antibody labels [38,39]. We explored the potential of NAD(P)H FLIM to separate out mature osteoclast that had been exposed to inflammatory cytokines by treating mature OC with 10 ng/mL TNFα for 1 hour before acquiring FLIM data. OC exposed to TNF-α for 1 hour seemed to have 2% higher of fraction bound NAD(P)H in the cytoplasm, but the difference might be to too low to look obvious in the FLIM images (figure 6 A, B).

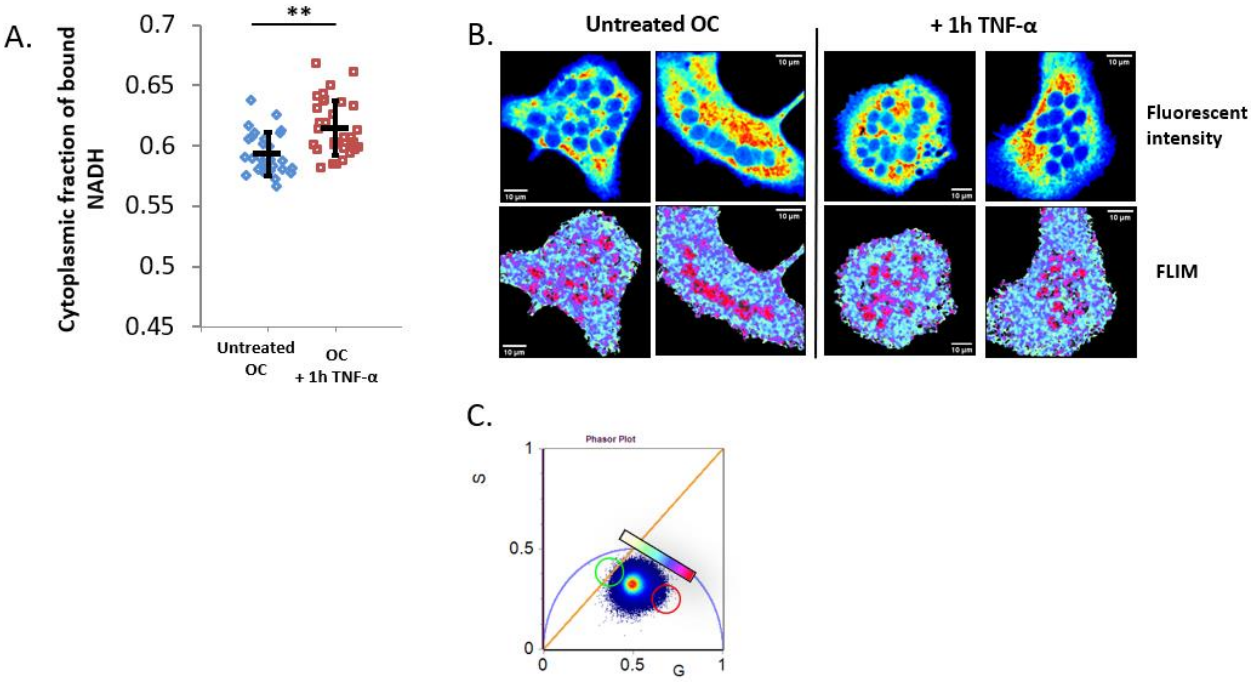

Figure 6: Effects of TNFα treatment on the NAD(P)H FLIM signal of mature osteoclast. Mature osteoclast on day 4 post RANKL stimulation were treated with 10 ng/mL of the inflammatory cytokine TNFα for 1 hour before NAD(P)H FLIM signal was acquired. A. fraction of bound NAD(P)H in the cytoplasm. B. Fluorescent intensity and FLIM images of some representative untreated control and TNFα treated cells. C. The phasor plot with the color scale for FLIM images. Mann-Whitney U test. *, $p < 0.05$; **, $p < 0.01$; ***, $p < 0.001$; ns, $p > 0.5$. n= 25-30 cells / group, two independent experiments.

2.6 Discussion

In view of the high energy demand during osteoclastogenic differentiation and bone resorption, we used NAD(P)H FLIM to examine the change of cellular metabolic profile throughout osteoclast differentiation. Our data indicated that cytoplasmic fraction of bound NAD(P)H decreased going from BMM to pOC and increased back up going from pOC to OC. Thus, it is probable that the differentiating cells shifted to a more glycolytic state, and the mature osteoclast cells shifted back to a more oxphos dominant state. That is reasonable since many glycolysis related genes such as *Hif1α* and glucose transporters are increasingly expressed after RANKL initiates differentiation [19]. Considering that cellular remodeling during differentiation is an energy demanding process, one might expect that cells would prefer mitochondrial oxphos, which is a more efficient method of making ATP [40]. Nevertheless, the rate of ATP production by glycolysis is faster despite not utilizing the full energy potential of each glucose molecule [41]. Unlike OCs, pOCs do not yet have the high number of fully developed mitochondria per nucleus[42], so they might have to increase glycolysis to keep up with their energetic needs. Moreover, increased demand for lipid and protein production during osteoclast differentiation might pull away intermediates of glycolysis and TCA cycle such as acetyl-CoA to participate in many anabolic pathways [43,44]. Thus, that would drive glycolytic reactions forward, further increasing the amount of free NADH. Upon reaching the OC stage, having increased number of mature mitochondria would allow cells to readily shift toward a more oxphos dominant metabolic program to satisfy their energetic needs.

Perturbation in iron transport and uptake is involved in many osteoclasts-mediated diseases [17,22,45]. Abnormal level of intercellular iron can alter the metabolic programing,

resulting in change in cell activity and signaling. We examined how iron transport perturbation can affect cellular metabolic profile at each stage of osteoclastogenesis by comparing NAD(P)H FLIM data of *fpn* KO and *tfr1* KO cells to WT cells. Our data indicated that the fraction bound NAD(P)H in the *fpn* KO and *tfr1* KO cytoplasm were higher and lower than WT cells respectively, but only at the pOC stage. It was as we expected that the increased intracellular iron in *fpn* KO cells would stimulate mitochondria activity, resulting in increased oxphos. However, it was surprising that we only saw this difference in only the pOC stage but not in BMM or OC. Likewise, NAD(P)H fraction bound in *tfr1* KO cells' cytoplasm was slightly lower than WT cells only in the pOC stage, suggesting that the mild iron starvation in *tfr1* KO made them more glycolytic than WT at the pOC stage. A possible explanation to why we only saw a difference at the pOC stage is that *fpn* and *tfr1* deletion would only alter the level of intracellular iron only during osteoclast differentiation. One should keep in mind that cellular need for iron uptake from the environment is relatively low, that over 90% of intracellular iron is recycled. Uptake from the environment only accounts for roughly 10% of the iron, and is only activated if cells really need iron [46]. The differentiating pOC cells most likely needed iron because of increased mitochondria biogenesis [47]. Furthermore, FPN is not the only factor that can decrease surplus intracellular iron, and TFR1 is not the only factor that mediate iron uptake (Figure 2). In the BMM and OC stages of *fpn* KO cells, ferritin storage and export might be able to sequester most of the excess iron despite lack of outward transport through FPN. However, enhanced iron uptake induced by iron regulatory protein 2 (IRP2) during osteoclast differentiation [47] might overwhelm ferritin storage, causing substantial increase in the level of intracellular iron relative to WT cells, and consequently increased oxphos. Similar explanation can be applied to the data

on TFR1 KO cells. At the BMM and OC stages, ferritin and heme uptake from the environment can make up for the loss of TFR1 mediated uptake (figure 2). However, enhanced need for iron during the pOC stage (characterized by IRP2 activation) might overwhelm ferritin and heme uptakes, resulting in a slight iron starvation in *tfr1* KO cells, and consequently a slight decrease in NAD(P)H fraction bound relative to WT. Though our data was indeed interesting, these explanations are in no way definitive without measuring intracellular iron and expression of all iron transport proteins at every stage of differentiation.

TNF-α is a proinflammatory factor that is known to be involved in bone destruction in rheumatoid arthritis and periodontal disease. It is established that exposure to TNFα after RANKL can accelerate osteoclast differentiation by further stimulating NF-κB pathway [4]. Recent studies from our collaborator and others had demonstrated that TNFα can also directly stimulate mature OC bone resorption activity like RANKL [5]. We were interested in knowing whether TNFα exposure can change the NAD(P)H FLIM signal of OCs. Our data showed that 1 hour of exposure to 10 ng/mL of TNF-a slightly increased fraction of bound NAD(P)H in the cytoplasm, suggesting that TNF-a might cause cells to shift to a more oxphos metabolic profile. Considering that TNF-α can participate in stimulating mature OCs bone resorption activity, which is energy demanding, OC cells might fulfill this increased need for ATP by enhancing oxphos. Additionally, TNFα is also capable to activating NADPH oxidase which create hydrogen peroxide using NADPH as energy, which might increase the fraction of bound NAD(P)H calculated through FLIM/phasor since it is still not possible to separate NADH and NADPH fluorescence signal. However, it is still unclear whether OCs express NADPH oxidase like its cousins, macrophage and dendritic cells. Nevertheless, we managed to distinguish OCs exposed

to TNFα from the untreated control without use of label or cell lysis.

2.7 Limitation of the study and future works

NADH and NADPH participate in distinct metabolic pathways, but it is still impossible to separate NADH and NADPH florescence from one another because they have the same spectrum and lifetimes. The intracellular concentration of NADH and NADPH might vary between cell types, and even cells in the same culture. In future studies, we will address this issue by using inhibitors that target either NADH or NADPH pathways and investigate how the FLIM data would change accordingly. Furthermore, our culturing condition might not be representative of the *in vivo* environment of osteoclasts. First, the majority of osteoclasts' bone remodeling compartment is on spongy bone, next to the bone marrow, which is relatively hypoxic with O_2 concentration around 3-4% [48]. Secondly, the bone matrix is completely different than the glass surface of our imaging dishes. Thus, we aim to implement hypoxia condition in our future experiments, and possibly grow cells on bone or dentine chips. However, bone chips might increase difficulty of finding cells and decrease resolving power.

2.8 Conclusion for chapter 2

In this study, we demonstrated that NAD(P)H FLIM coupled with phasor analysis can be a practical method to dynamically investigate cellular metabolic profile throughout osteoclastogenesis without labels or cell lysis. During osteoclast differentiation, cells seemed to shift toward glycolysis and then shifted back toward oxphos upon reaching maturation. Iron transport perturbation via *ferroportin* or *transferrin receptor 1* deletion seemed to cause a shift in metabolism toward oxphos and glycolysis respectively, but only during differentiation. Finally, we also managed to distinguish mature osteoclasts exposed to TNFα from untreated

controls, suggesting that NAD(P)H FLIM/phasor might even have the potential study inflammatory bones destruction without antibody labels, unlike conventional assays.

Chapter 3: The study on membrane fluidity during osteoclastogenesis using Spectral imaging and LAUDAN.

3.1 Introduction

Cholesterol, the molecule that involved in controlling the viscosity of cell membranes, might have a critical role in osteoclast differentiation and function. One analysis of clinical data demonstrated that there could be an association between osteoporosis and high serum cholesterol although the correlation is inconsistent and varies between groups of patients [49]. However, obese patients who administered the serum cholesterol lowering drug Statin seemed to recover bone density and have reduced risk of bone fracture [50]. Sequestering cholesterol in the differentiating pre-osteoclast cells *in vitro* using MCD (methyl-β-cyclodextrine) disrupts cells fusion and promotes apoptosis. In mature osteoclast culture, MCD treatment interferes with actin ring formation, resulting in non-functional resorption zones and also mature osteoclast apoptosis [51,52]. In contrast, supplementation of cholesterol to osteoclast culture in vitro promotes survival and function [52]. Fatostatin, an inhibitor of sterol regulatory element binding protein (SREBP), was found to decrease RANKL-induced bone loss in mice by preventing osteoclast differentiation [53]. SREBP is a master controller of both lipid and cholesterol synthesis. Activated SREBP increases expression of proteins associated with cholesterol and fatty acid synthesis [54].

Given that lipids, especially cholesterol, might have an important role in osteoclast differentiation and function, in this part of the thesis I set out to investigate how the fluidity of membrane would change though out the course of osteoclast differentiation. Knowing more about membrane dynamics would allow us to design better therapeutic strategies in the future, while batter understand the pathogenesis of osteoclasts-mediated diseases. For this purpose, I used the fluorescent probe LAURDAN. This probe has been used extensively to study the fluidity of the cell membrane because of its unique ability to sense the polarity of its surrounding, while its hydrophobic tail allows the LAURDAN molecule to rapidly accumulate in the lipid bilayer (figure 7C). Coupled with spectral microscopy and phasor analysis, we can quickly examine membrane fluidity of cells in the single cell level, unlike other techniques that involve destruction of the entire cell culture. My preliminary data suggested that cellular membranes became more solid as cells differentiate toward mature osteoclast.

3.2 Spectral phasor and LAURDAN

In spectral imaging microscopy, the spectral information at each pixel is collected by first passing the emitted light through either a prism or a diffraction grating. Like fluorescence lifetime, the phasor approach can be used to describe the spectrum at each pixel. The spectrum at each pixel can be transformed into the phasor space using the following equations:

$$G(\lambda) = \frac{\int_{\lambda min}^{\lambda max} I(\lambda)\cos\left(\frac{2\pi n(\lambda - \lambda_i)}{\lambda max - \lambda min}\right)d\lambda}{\int_{\lambda min}^{\lambda max} I(\lambda)d\lambda}$$

$$S(\lambda) = \frac{\int_{\lambda min}^{\lambda max} I(\lambda)\sin\left(\frac{2\pi n(\lambda - \lambda_i)}{\lambda max - \lambda min}\right)d\lambda}{\int_{\lambda min}^{\lambda max} I(\lambda)d\lambda}$$

On the spectral phasor plot, wavelength increases in the counterclockwise direction while the distance of a pixel from the center of the plot is proportional to the width of the its spectrum (figure 7 A,B).

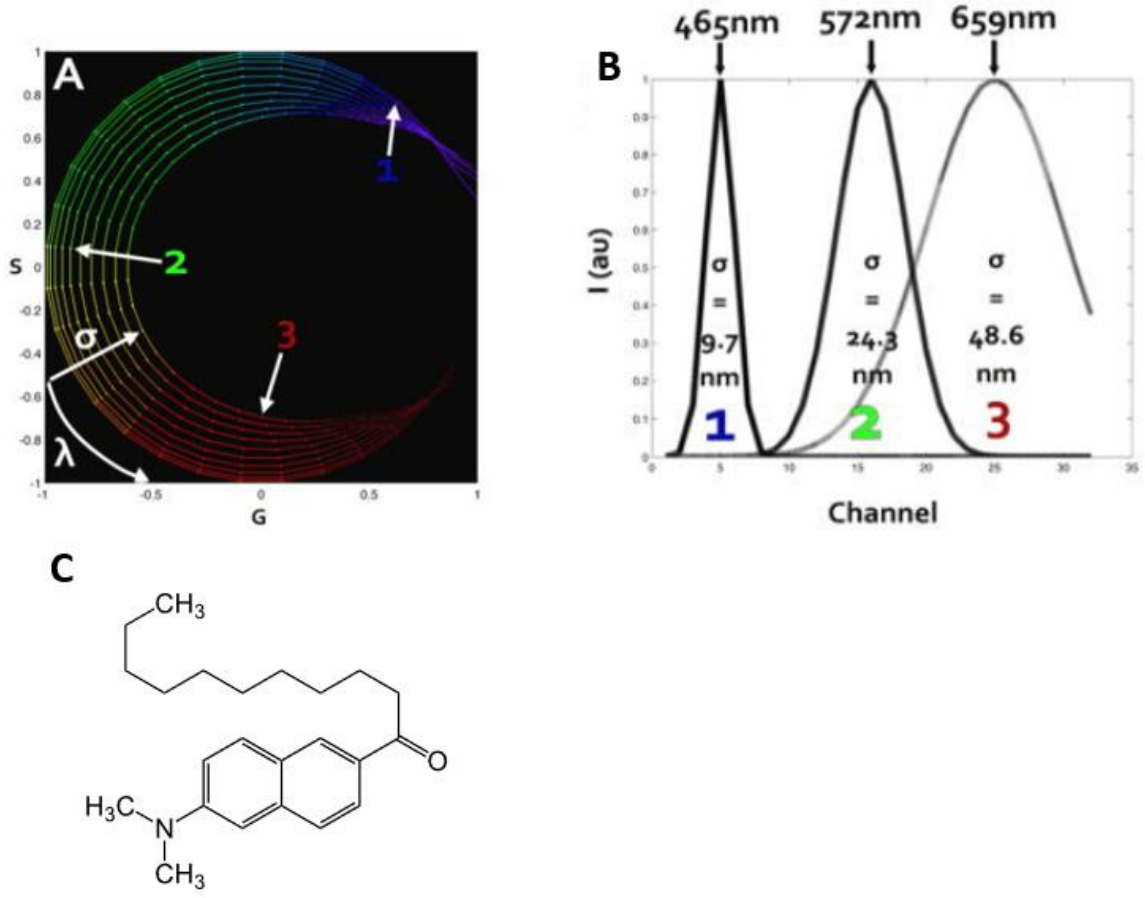

Figure 7: LAURDAN and spectral imaging. Spectral phasor graph and the molecular structure of LAURDAN. A and B. Phasor positions and their equivalent spectra from Cutrale et al [55]. C. LAURDAN molecular structure.

LAURDAN (6-dodecanoyl-2-dimethylaminonaphthalene) is a molecule belonging to the family dimethyaminonaphthalene (Figure 7C). Light excitation can cause the dipole moment of LAURDAN molecules to greatly increase, that it can reorient the other polar molecules in the surrounding environment. Spending energy on reorienting the surrounding molecules causes

the emission spectrum of LAURDAN to shift toward red, longer wavelength [56]. The LAURDAN molecule also possesses a hydrophobic tail which would allow the molecule to rapidly integrate into the lipid bilayer, making it possible to examine water penetration, a property related to the physical phase of the membrane. In a pure liquid order (lo) membrane, LAURDAN emission centers around 440 nm. However, a liquid disorder (ld) membrane would allow water molecules to penetrate inside, which is sensed by the LAURDAN molecule upon excitation, resulting in a 50 nm red shift [57,58]. Cell membrane fluidity is determined by both the lipid composition and cholesterol. Prior studies showed that imaging with LAURDAN can distinguish between artificial DPPC vesicles with different cholesterol concentration [57,59]. When coupled with spectral phasor analysis, LAURDAN can also distinguish cell membranes in a multitude of physiological conditions [60,61]. Thus, it might be useful in examining the change of membrane fluidity during osteoclastogenesis, allowing us to indirectly have a deeper understanding of the role cholesterol and other lipids have in osteoclasts-mediated diseases.

3.3 Materials and methods

Osteoclast culture and differentiation

Cells were collected, cultured, and stimulated in the same way as chapter 2.

LAURDAN treatment and spectral imaging

Spectral fluorescence data was collected using the Lamda mode configuration of Zeiss LSM 710 laser scanning microscope (Carl Zeiss, Dublin, CA-USA) equipped with a Ti: Sapphire laser (Spectra-Physics Mai Tai, Newport Beach CA-USA). The Lamda mode was configured in 32 channels, each has a bandwidth of 9.7 nm and the total range from 416 to 728 nm. Frame size

was 256x256 and the pixel dwell time was 5.09 µs / pixels. Cells were treated with 1 uM LAURDAN 30 minutes before imaging. To excite LAURDAN, the excitation laser wavelength was adjusted to 780 nm (2 photons excitation). A 40x water objective from Zeiss was used for capturing of all images. The spectral LSM file was transformed into phasor using the the program SimFCS developed at the Laboratory for Fluorescence Dynamics. One image was taken with the laser off to be used for background subtraction in SimFCS.

3.4 Preliminary results

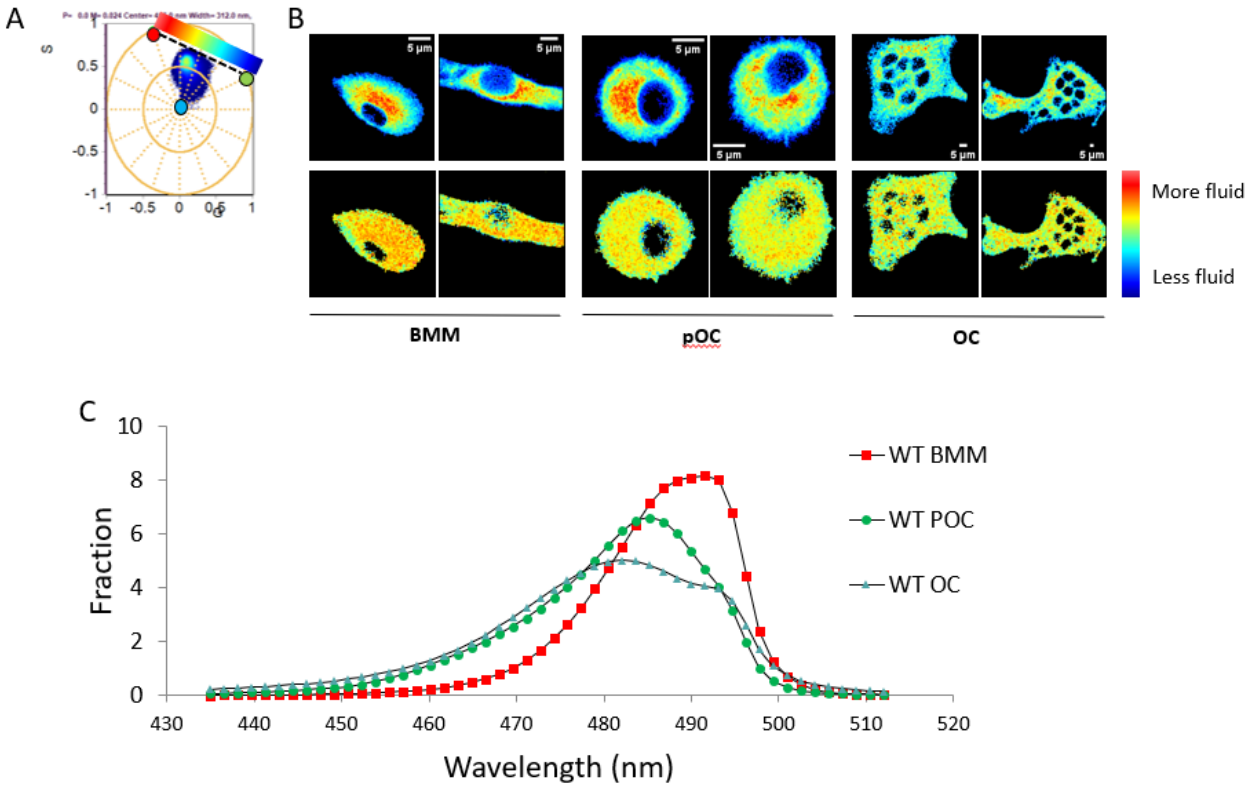

Figure 8: LAURDAN fluorescence during osteoclast differentiation. A. the phasor cloud of the entire experiment, blue cursor was placed in the center of the phasor plot, green and red cursor was placed on the circle at 435 and 520 nm wavelength respectively. B. Representative images, first row is LAURDAN intensity image, second row is the fluidity image constructed by placing a color scale on top of the line connecting red to green cursor. C. the spectrum of LAURDAN on the membrane of the entire cells from each group (BMM, pOC, OC) by projecting the phasor

cloud of the entire group onto the red-green line, which goes from 430 nm to 520 nm. n = 6 cells / group.

To analyze the phasor plot, we used the three components analysis approach, in which one cursor is placed on the center (background) and two were placed on the circle at 435 nm and 520 nm (Figure 8A). The phasor cloud of all the cells in the experiment lie within the triangle formed by the three cursors. Then, using SimFCS, the phasor cloud was projected onto the red-green line. The fluidity image was constructed by placing a color scale on top of the red-green cursor line. On the color scale, red was the most fluid while blue was the most solid (Figure 8 A, B). If the LAURDAN spectrum of a pixel is closer to the green cursor, the LAURDAN molecules inside this pixel was inside a more aqueous membrane. Fluidity images in figure B showed that BMMs had more red and orange pixels than either pOCs or OCs, suggesting that the total membrane of BMM was more fluid. There seemed to be no obvious difference between pOC and OC cells. Instead of selecting all the cells in the experiment, one single group of cells (e.g. BMM) can be selected on SimFCS, and the phasor cloud of this group can be projected on to the red-green cursor line. The resulting histogram is a spectrum that sums up the LAURDAN spectra of the entire group (figure 8C). As cells differentiate from BMM to pOC and OC, the average LAURDAN spectra seemed to slightly shift toward a shorter wavelength, suggesting that pOCs an OCs has higher total membrane viscosity.

3.5 Discussion

Increasing amount of evidence has demonstrated the importance of cholesterol and lipids in osteoclast differentiation and function. Because lipid composition and especially presence of cholesterol are critical in determining the dynamics of the cell membranes. In this study, we aimed at investigating the possible change of membrane fluidity during osteoclast

differentiation using LAURDAN coupled with spectral imaging and phasor analysis. Our preliminary data indicated that the average spectrum of LAURDAN in pOC and OC cells shifted toward the blue side relative to LAURDAN in BMM, suggesting that the total membranes of pOC and OC cells might be more solid than the membranes of BMM. It should emphasized that the LAURDAN spectrum and fluidity images in our preliminary study are representative of the cell total membrane. Though it would be more ideal to observe the plasma membrane or organelle membrane separately, we could not resolve individual membrane because the thickness of phospholipid bilayer is about 10 nm, well below the resolving power of 366 nm in our current setup. This issue will be addressed in the future by using other imaging modalities that increase resolving power such total internal reflection fluorescence microscopy (TIRF) or super resolution microscopy in future experiments. However, preliminary data on total membrane fluidity would at least give us some clue about change in physical property of cells' membranes as they differentiate toward mature OCs. It was as we expected that OCs would have more solid membranes because these are very large cells (up to 150 um in diameter), thus their membranes might need to be rigid to maintain its massive structure. The increase in membrane solidity can also be attributed to increase in lipid rafts, which are microdomains packed full of cholesterol [62]. The lipid raft marker flotillin was found to have substantially increased expression during and after osteoclast differentiation[51]. OCs contain a large amount of different membrane transporters on either the bone resorption side or the basolateral side of their plasma membrane [63]. Attaching to lipid rafts might ensure proper function of membrane transporters by limiting lateral diffusion, allowing them to stay on their proper side of the membrane. Lipid rafts on the endoplasmic reticulum might have increased in pOC and OC as

well, because the liquidity images seems to show that most of the different in fluidity was inside the cells (figure B). It might be reasonable considering that the membrane transporters are form on the ER and constantly shuttled onto the plasma membrane via vesicles.

3.6 Conclusion and future works

In this study, we demonstrated that cellular total membranes became less fluid as they differentiate from bone marrow monocyte, to pre-osteoclasts, and mature osteoclast via LAURDAN spectral imaging coupled with phasor analysis. Knowing more about changes in membrane fluidity will allow us to indirectly better understand the role of cholesterol and lipid rafts in proper osteoclast function. Besides moving to different imaging platforms like TIRF and STED for better resolving power, we can also investigate how cholesterol sequestering compounds affect the membrane fluidity of osteoclasts in the future.

References:

(1) Khosla, S.; Westendorf, J. J.; Mödder, U. I. Concise Review: Insights from Normal Bone Remodeling and Stem Cell-Based Therapies for Bone Repair. *Stem Cells* **2010**, *28* (12), 2124–2128. https://doi.org/10.1002/stem.546.

(2) Boyle, W. J.; Simonet, W. S.; Lacey, D. L. Osteoclast Differentiation and Activation. *Nature* **2003**, *423* (6937), 337–342. https://doi.org/10.1038/nature01658.

(3) Takeshita, S.; Kaji, K.; Kudo, A. Identification and Characterization of the New Osteoclast Progenitor with Macrophage Phenotypes Being Able to Differentiate into Mature Osteoclasts. *Journal of Bone and Mineral Research* **2000**, *15* (8), 1477–1488. https://doi.org/10.1359/jbmr.2000.15.8.1477.

(4) Zhang, Y.-H.; Heulsmann, A.; Tondravi, M. M.; Mukherjee, A.; Abu-Amer, Y. Tumor Necrosis Factor-α (TNF) Stimulates RANKL-Induced Osteoclastogenesis via Coupling of TNF Type 1 Receptor and RANK Signaling Pathways. *J. Biol. Chem.* **2001**, *276* (1), 563–568. https://doi.org/10.1074/jbc.M008198200.

(5) Fuller, K.; Murphy, C.; Kirstein, B.; Fox, S. W.; Chambers, T. J. TNFα Potently Activates Osteoclasts, through a Direct Action Independent of and Strongly Synergistic with RANKL. *Endocrinology* **2002**, *143* (3), 1108–1118. https://doi.org/10.1210/endo.143.3.8701.

(6) Xu, F.; Teitelbaum, S. L. Osteoclasts: New Insights. *Bone Res.* **2013**, *1* (1), 11–26. https://doi.org/10.4248/BR201301003.

(7) Vander Heiden, M. G.; Cantley, L. C.; Thompson, C. B. Understanding the Warburg Effect: The Metabolic Requirements of Cell Proliferation. *Science* **2009**, *324* (5930), 1029–1033. https://doi.org/10.1126/science.1160809.

(8) Karner, C. M.; Long, F. Glucose Metabolism in Bone. *Bone* **2018**, *115*, 2–7. https://doi.org/10.1016/j.bone.2017.08.008.

(9) Arnett, T. R.; Orriss, I. R. Metabolic Properties of the Osteoclast. *Bone* **2018**, *115*, 25–30. https://doi.org/10.1016/j.bone.2017.12.021.

(10) Ahn, H.; Lee, K.; Kim, J. M.; Kwon, S. H.; Lee, S. H.; Lee, S. Y.; Jeong, D. Accelerated Lactate Dehydrogenase Activity Potentiates Osteoclastogenesis via NFATc1 Signaling. *PLoS ONE* **2016**, *11* (4), e0153886. https://doi.org/10.1371/journal.pone.0153886.

(11) Wei, W.; Wang, X.; Yang, M.; Smith, L. C.; Dechow, P. C.; Wan, Y. PGC1β Mediates PPARγ Activation of Osteoclastogenesis and Rosiglitazone-Induced Bone Loss. *Cell Metabolism* **2010**, *11* (6), 503–516. https://doi.org/10.1016/j.cmet.2010.04.015.

(12) Lemma, S.; Sboarina, M.; Porporato, P. E.; Zini, N.; Sonveaux, P.; Di Pompo, G.; Baldini, N.; Avnet, S. Energy Metabolism in Osteoclast Formation and Activity. *The International Journal of Biochemistry & Cell Biology* **2016**, *79*, 168–180. https://doi.org/10.1016/j.biocel.2016.08.034.

(13) Demianova, Z.; Cox, D.; Gorre, E.; Xiong, L. Quantitative and Qualitative Analysis of Cell Culture Medium Using SWATH® Acquisition. 7.

(14) Plitzko, B.; Loesgen, S. Measurement of Oxygen Consumption Rate (OCR) and Extracellular Acidification Rate (ECAR) in Culture Cells for Assessment of the Energy Metabolism. *BIO-PROTOCOL* **2018**, *8* (10). https://doi.org/10.21769/BioProtoc.2850.

(15) He, H.; Qiao, Y.; Zhou, Q.; Wang, Z.; Chen, X.; Liu, D.; Yin, D.; He, M. Iron Overload Damages the Endothelial Mitochondria via the ROS/ADMA/DDAHII/eNOS/NO Pathway https://www.hindawi.com/journals/omcl/2019/2340392/ (accessed May 1, 2020). https://doi.org/10.1155/2019/2340392.

(16) Murphy, M. P.; Holmgren, A.; Larsson, N.-G.; Halliwell, B.; Chang, C. J.; Kalyanaraman, B.; Rhee, S. G.; Thornalley, P. J.; Partridge, L.; Gems, D.; Nyström, T.; Belousov, V.; Schumacker, P. T.;

Winterbourn, C. C. Unraveling the Biological Roles of Reactive Oxygen Species. *Cell Metabolism* **2011**, *13* (4), 361–366. https://doi.org/10.1016/j.cmet.2011.03.010.
(17) Balogh, E.; Paragh, G.; Jeney, V. Influence of Iron on Bone Homeostasis. *Pharmaceuticals (Basel)* **2018**, *11* (4). https://doi.org/10.3390/ph11040107.
(18) Kasvosve, I.; Debebe, Z.; Nekhai, S.; Gordeuk, V. R. Ferroportin (SLC40A1) Q248H Mutation Is Associated with Lower Circulating Plasma Tumor Necrosis Factor-α and Macrophage Migration Inhibitory Factor Concentrations in African Children. *Clin Chim Acta* **2010**, *411* (17–18), 1248–1252. https://doi.org/10.1016/j.cca.2010.04.031.
(19) Wang, L.; Fang, B.; Fujiwara, T.; Krager, K.; Gorantla, A.; Li, C.; Feng, J. Q.; Jennings, M. L.; Zhou, J.; Aykin-Burns, N.; Zhao, H. Deletion of Ferroportin in Murine Myeloid Cells Increases Iron Accumulation and Stimulates Osteoclastogenesis in Vitro and in Vivo. *J. Biol. Chem.* **2018**, *293* (24), 9248–9264. https://doi.org/10.1074/jbc.RA117.000834.
(20) Manara, M.; Sinigaglia, L. Bone and TNF in Rheumatoid Arthritis: Clinical Implications. *RMD Open* **2015**, *1* (Suppl 1), e000065. https://doi.org/10.1136/rmdopen-2015-000065.
(21) Graves, D. T.; Cochran, D. The Contribution of Interleukin-1 and Tumor Necrosis Factor to Periodontal Tissue Destruction. *J. Periodontol.* **2003**, *74* (3), 391–401. https://doi.org/10.1902/jop.2003.74.3.391.
(22) Dev, S.; Babitt, J. L. Overview of Iron Metabolism in Health and Disease. *Hemodialysis International* **2017**, *21* (S1), S6–S20. https://doi.org/10.1111/hdi.12542.
(23) Stringari, C.; Nourse, J. L.; Flanagan, L. A.; Gratton, E. Phasor Fluorescence Lifetime Microscopy of Free and Protein-Bound NADH Reveals Neural Stem Cell Differentiation Potential. *PLoS ONE* **2012**, *7* (11), e48014. https://doi.org/10.1371/journal.pone.0048014.
(24) Stringari, C.; Wang, H.; Geyfman, M.; Crosignani, V.; Kumar, V.; Takahashi, J. S.; Andersen, B.; Gratton, E. In Vivo Single Cell Detection of Metabolic Oscillations in Stem Cells. *Cell Rep* **2015**, *10* (1), 1–7. https://doi.org/10.1016/j.celrep.2014.12.007.
(25) Ranjit, S.; Malacrida, L.; Jameson, D. M.; Gratton, E. Fit-Free Analysis of Fluorescence Lifetime Imaging Data Using the Phasor Approach. *Nat Protoc* **2018**, *13* (9), 1979–2004. https://doi.org/10.1038/s41596-018-0026-5.
(26) Digman, M. A.; Caiolfa, V. R.; Zamai, M.; Gratton, E. The Phasor Approach to Fluorescence Lifetime Imaging Analysis. *Biophysical Journal* **2008**, *94* (2), L14–L16. https://doi.org/10.1529/biophysj.107.120154.
(27) Zhao, Y.; Yang, Y.; Loscalzo, J. Real Time Measurement of Metabolic States in Living Cells Using Genetically-Encoded NADH Sensors. *Methods Enzymol* **2014**, *542*, 349–367. https://doi.org/10.1016/B978-0-12-416618-9.00018-2.
(28) NAD/NADH-Glo™ Assay Protocol https://www.promega.com/resources/protocols/technical-manuals/101/nad-nadh-glo-assay-protocol/ (accessed May 4, 2020).
(29) NAD/NADH Cell-Based Assay Kit https://www.caymanchem.com/product/600480 (accessed May 4, 2020).
(30) Schaefer, P. M.; Kalinina, S.; Rueck, A.; Arnim, C. A. F. von; Einem, B. von. NADH Autofluorescence—A Marker on Its Way to Boost Bioenergetic Research. *Cytometry Part A* **2019**, *95* (1), 34–46. https://doi.org/10.1002/cyto.a.23597.
(31) Huang, S.; Heikal, A. A.; Webb, W. W. Two-Photon Fluorescence Spectroscopy and Microscopy of NAD(P)H and Flavoprotein. *Biophysical Journal* **2002**, *82* (5), 2811–2825. https://doi.org/10.1016/S0006-3495(02)75621-X.
(32) Hull, R. V.; Conger, P. S.; Hoobler, R. J. Conformation of NADH Studied by Fluorescence Excitation Transfer Spectroscopy. *Biophysical Chemistry* **2001**, *90* (1), 9–16. https://doi.org/10.1016/S0301-4622(00)00239-8.

(33) König, K.; So, P. T. C.; Mantulin, W. W.; Tromberg, B. J.; Gratton, E. Two-Photon Excited Lifetime Imaging of Autofluorescence in Cells during UV A and NIR Photostress. *Journal of Microscopy* **1996**, *183* (3), 197–204. https://doi.org/10.1046/j.1365-2818.1996.910650.x.
(34) Wright, B. K.; Andrews, L. M.; Jones, M. R.; Stringari, C.; Digman, M. A.; Gratton, E. Phasor-Flim Analysis of NADH Distribution and Localization in the Nucleus of Live Progenitor Myoblast Cells. *Microsc. Res. Tech.* **2012**, *75* (12), 1717–1722. https://doi.org/10.1002/jemt.22121.
(35) Adamopoulos, I. E. Inflammation in Bone Physiology and Pathology: *Current Opinion in Rheumatology* **2018**, *30* (1), 59–64. https://doi.org/10.1097/BOR.0000000000000449.
(36) Luo, G.; Li, F.; Li, X.; Wang, Z.-G.; Zhang, B. TNF-α and RANKL Promote Osteoclastogenesis by Upregulating RANK via the NF-KB Pathway. *Mol Med Rep* **2018**, *17* (5), 6605–6611. https://doi.org/10.3892/mmr.2018.8698.
(37) Kobayashi, K.; Takahashi, N.; Jimi, E.; Udagawa, N.; Takami, M.; Kotake, S.; Nakagawa, N.; Kinosaki, M.; Yamaguchi, K.; Shima, N.; Yasuda, H.; Morinaga, T.; Higashio, K.; Martin, T. J.; Suda, T. Tumor Necrosis Factor Alpha Stimulates Osteoclast Differentiation by a Mechanism Independent of the ODF/RANKL-RANK Interaction. *J. Exp. Med.* **2000**, *191* (2), 275–286. https://doi.org/10.1084/jem.191.2.275.
(38) Ma, N.; Mochel, N. R. de; Pham, P. D.; Yoo, T. Y.; Cho, K. W. Y.; Digman, M. A. Label-Free Assessment of Pre-Implantation Embryo Quality by the Fluorescence Lifetime Imaging Microscopy (FLIM)-Phasor Approach. *Sci Rep* **2019**, *9* (1), 1–13. https://doi.org/10.1038/s41598-019-48107-2.
(39) Alfonso-García, A.; Smith, T. D.; Datta, R.; Luu, T. U.; Gratton, E.; Potma, E. O.; Liu, W. F. Label-Free Identification of Macrophage Phenotype by Fluorescence Lifetime Imaging Microscopy. *J. Biomed. Opt* **2016**, *21* (4), 046005. https://doi.org/10.1117/1.JBO.21.4.046005.
(40) Berg, J. M.; Tymoczko, J. L.; Stryer, L. Metabolism Consist of Highly Interconnected Pathways. *Biochemistry. 5th edition* **2002**.
(41) Jose, C.; Bellance, N.; Rossignol, R. Choosing between Glycolysis and Oxidative Phosphorylation: A Tumor's Dilemma? *Biochimica et Biophysica Acta (BBA) - Bioenergetics* **2011**, *1807* (6), 552–561. https://doi.org/10.1016/j.bbabio.2010.10.012.
(42) Brown, D.; Breton, S. Mitochondria-Rich, Proton-Secreting Epithelial Cells. *Journal of Experimental Biology* **1996**, *199* (11), 2345–2358.
(43) Mashima, T.; Seimiya, H.; Tsuruo, T. De Novo Fatty-Acid Synthesis and Related Pathways as Molecular Targets for Cancer Therapy. *Br J Cancer* **2009**, *100* (9), 1369–1372. https://doi.org/10.1038/sj.bjc.6605007.
(44) Chapter 21 : Biosynthesis of Amino Acids, Nucleotides, and Related Molecules http://www.bioinfo.org.cn/book/biochemistry/chapt21/bio3.htm (accessed May 18, 2020).
(45) Jeney, V. Clinical Impact and Cellular Mechanisms of Iron Overload-Associated Bone Loss. *Front. Pharmacol.* **2017**, *8*. https://doi.org/10.3389/fphar.2017.00077.
(46) Drakesmith, H.; Nemeth, E.; Ganz, T. Ironing out Ferroportin. *Cell Metabolism* **2015**, *22* (5), 777–787. https://doi.org/10.1016/j.cmet.2015.09.006.
(47) Ishii, K.; Fumoto, T.; Iwai, K.; Takeshita, S.; Ito, M.; Shimohata, N.; Aburatani, H.; Taketani, S.; Lelliott, C. J.; Vidal-Puig, A.; Ikeda, K. Coordination of PGC-1β and Iron Uptake in Mitochondrial Biogenesis and Osteoclast Activation. *Nat Med* **2009**, *15* (3), 259–266. https://doi.org/10.1038/nm.1910.
(48) Nombela-Arrieta, C.; Silberstein, L. E. The Science behind the Hypoxic Niche of Hematopoietic Stem and Progenitors. *Hematology Am Soc Hematol Educ Program* **2014**, *2014* (1), 542–547. https://doi.org/10.1182/asheducation-2014.1.542.

(49) Makovey, J.; Chen, J. S.; Hayward, C.; Williams, F. M. K.; Sambrook, P. N. Association between Serum Cholesterol and Bone Mineral Density. *Bone* **2009**, *44* (2), 208–213. https://doi.org/10.1016/j.bone.2008.09.020.
(50) Edwards, C. J.; Spector, T. D. Statins as Modulators of Bone Formation. 3.
(51) Ha, H.; Kwak, H. B.; Lee, S. K.; Na, D. S.; Rudd, C. E.; Lee, Z. H.; Kim, H.-H. Membrane Rafts Play a Crucial Role in Receptor Activator of Nuclear Factor KB Signaling and Osteoclast Function. *J. Biol. Chem.* **2003**, *278* (20), 18573–18580. https://doi.org/10.1074/jbc.M212626200.
(52) Luegmayr, E.; Glantschnig, H.; Wesolowski, G. A.; Gentile, M. A.; Fisher, J. E.; Rodan, G. A.; Reszka, A. A. Osteoclast Formation, Survival and Morphology Are Highly Dependent on Exogenous Cholesterol/Lipoproteins. *Cell Death Differ* **2004**, *11* (1), S108–S118. https://doi.org/10.1038/sj.cdd.4401399.
(53) Inoue, K.; Imai, Y. Fatostatin, an SREBP Inhibitor, Prevented RANKL-Induced Bone Loss by Suppression of Osteoclast Differentiation. *Biochimica et Biophysica Acta (BBA) - Molecular Basis of Disease* **2015**, *1852* (11), 2432–2441. https://doi.org/10.1016/j.bbadis.2015.08.018.
(54) Krycer, J. R.; Sharpe, L. J.; Luu, W.; Brown, A. J. The Akt–SREBP Nexus: Cell Signaling Meets Lipid Metabolism. *Trends in Endocrinology & Metabolism* **2010**, *21* (5), 268–276. https://doi.org/10.1016/j.tem.2010.01.001.
(55) Cutrale, F.; Salih, A.; Gratton, E. Spectral Phasor Approach for Fingerprinting of Photo-Activatable Fluorescent Proteins Dronpa, Kaede and KikGR. *Method Appl Fluoresc* **2013**, *1* (3), 035001. https://doi.org/10.1088/2050-6120/1/3/035001.
(56) Weber, G.; Farris, F. J. Synthesis and Spectral Properties of a Hydrophobic Fluorescent Probe: 6-Propionyl-2-(Dimethylamino)Naphthalene. *Biochemistry* **1979**, *18* (14), 3075–3078. https://doi.org/10.1021/bi00581a025.
(57) Parasassi, T.; De Stasio, G.; d'Ubaldo, A.; Gratton, E. Phase Fluctuation in Phospholipid Membranes Revealed by Laurdan Fluorescence. *Biophys J* **1990**, *57* (6), 1179–1186.
(58) Sanchez, S. A.; Tricerri, M. A.; Gratton, E. Laurdan Generalized Polarization Fluctuations Measures Membrane Packing Micro-Heterogeneity in Vivo. *PNAS* **2012**, *109* (19), 7314–7319. https://doi.org/10.1073/pnas.1118288109.
(59) Harris, F. M.; Best, K. B.; Bell, J. D. Use of Laurdan Fluorescence Intensity and Polarization to Distinguish between Changes in Membrane Fluidity and Phospholipid Order. *Biochimica et Biophysica Acta (BBA) - Biomembranes* **2002**, *1565* (1), 123–128. https://doi.org/10.1016/S0005-2736(02)00514-X.
(60) Malacrida, L.; Jameson, D. M.; Gratton, E. A Multidimensional Phasor Approach Reveals LAURDAN Photophysics in NIH-3T3 Cell Membranes. *Sci Rep* **2017**, *7* (1), 1–11. https://doi.org/10.1038/s41598-017-08564-z.
(61) Sameni, S.; Malacrida, L.; Tan, Z.; Digman, M. A. Alteration in Fluidity of Cell Plasma Membrane in Huntington Disease Revealed by Spectral Phasor Analysis. *Sci Rep* **2018**, *8* (1), 1–10. https://doi.org/10.1038/s41598-018-19160-0.
(62) Simons, K.; Ehehalt, R. Cholesterol, Lipid Rafts, and Disease. *J Clin Invest* **2002**, *110* (5), 597–603. https://doi.org/10.1172/JCI16390.
(63) Baron, R. Polarity and Membrane Transport in Osteoclasts. *Connective Tissue Research* **1989**, *20* (1–4), 109–120. https://doi.org/10.3109/03008208909023879.